Coseismic Landsliding associated with the April-May 2015 Gorkha Earthquake Sequence, Nepal

Abstract

Coseismic landsliding poses immediate and prolonged hazards to mountainous communities, as well as a rare opportunity to study the effect of large earthquakes on erosion and sediment budgets. The April-May 2015 Gorkha earthquake sequence was associated with widespread landsliding throughout the steep Himalayan Mountains in central Nepal. To investigate the effects of seismic shaking on slope stability, landslides were manually mapped using high-resolution pre- and post-event satellite imagery. Landslide activity appears to be associated mainly with the M_w7.8 main shock on April 25, with only minor additional landsliding due to the M_w7.2 May 12 aftershock. The observed distribution shows the greatest density of landsliding at 1500-3500 m elevation in Greater Himalayan river gorges. This density pattern may reflect variations in rock strength with elevation, and possibly local variations in PGA due to topographic effects. Landslide density is highest above the eastern end of the fault rupture area, which mirrors a focusing of energy from the April 25 mainshock in the direction of rupture propagation. Landslide mobility was also calculated as a function of the ratio of drop height to runout length versus landslide volume. It was found that the most mobile landslides tended to occur at >3500 m elevation in the Greater Himalaya, which may reflect lower frictional resistance to landslide movement at higher elevations due to ice and snow, a tendency to observe larger source areas at high elevations, or steeper, longer hillslopes at high elevations.

Introduction

Coseismic landslides have long been recognized as an important secondary hazard of earthquakes. They can contribute heavily to observed losses, as in the 2008 Wenchuan earthquake, where about 20,000 of 100,000 fatalities were attributed directly to landsliding (*Huang et al.,* 2013). Coseismic landsliding is also thought to contribute to erosional budgets in mountain belts over geologic timescales (*Parker et al.,* 2011), and an important factor in creating steep, irregular hillslopes in active mountain belts (*Densmore et al.,* 1997). Additionally, coseismic landslide distributions can be used with modeled PGA distributions from earthquakes to investigate variations in surface-forming material strength across landscapes (*Gallen et al.,* 2015).

The magnitudes of coseismic landslide events are observed to follow a power-law relation with the associated earthquake moment magnitude (*Malamud and Turcotte*, 2004; *Keefer*, 1984). However, this relationship is likely biased towards conditions favoring higher event magnitudes, such as steep topography and occurrence of the event on a shallow continental fault, because landslide events that are typically large enough to study occur under these conditions. The distribution of coseismic landsliding is influenced by factors such as PGA and local hillslope steepness (*Keefer,* 1984*; Meunier et al.,* 2009). Because coseismic landslides involve movement of material in the upper tens of meters of the ground surface, variations in near-surface material strength can influence landslide distribution as well. These strength contrasts might arise from varying weathering processes and lithologies across the affected area, as well as groundwater presence.

Coseismic landslides encompass a range of landslide movement types and typically involve both rock and soil. These can be broadly classified by five categories of movement and material type, including coherent slides in soil, coherent slides in rock, disrupted slides

and falls in soil, disrupted slides and falls in rock, and lateral spreads (*Keefer*, 1984). Categories are distinguished by the nature of the material the slide occurs in, and the presence or lack of internal deformation in the landslide mass (*Varnes*, 1978). In this system, "rock" is considered to be largely intact bedrock, while "soils" include essentially the entire range of materials classified as "regolith", including saprolite (weathered, fractured bedrock) and unconsolidated sediment and soils.

Coherent slides are generally deep-seated movements of blocks of material with relatively little internal deformation. These landslides form a curved or linear detachment surface, above which intact material is displaced. The form of a detachment surface, and coherent movement are typically controlled to a large extent by features such as soil horizons, saturated layers, and planes of foliation or bedding in rock. In contrast, disrupted slides involve more fracturing and fluid-like movement of the landslide mass. Disrupted slides typically develop on steeper slopes than coherent slides and involve fast, energetic movements of material. Lateral spreads involve largely translational movement of material over a saturated layer. Lateral spreads occur only in unconsolidated surface materials, can happen at very shallow slopes, and can be fast and energetic. In general, the vast majority of landslides triggered by earthquakes are disrupted rock or soil slides. Coherent slides and lateral spreads are relatively rare (*Keefer,* 2002).

Himalayan seismotectonics and the 2015 M7.8 Gorkha earthquake sequence

The Himalayan front has long been recognized as an area of high seismic hazard. Active continental convergence of India and Asia occurs at a rate of about 45 mm/yr (*Sella et al*., 2002), of which 20 mm/yr is accommodated by the Main Himalayan Thrust (*Lavé and Avouac,* 2000). Earthquakes on this fault have included probable M8-9 events in the past, such as a large earthquake in 1505 *(Bilham,* 2003). However, only intermediate-magnitude earthquakes have occurred in Nepal in the last century, such as the 1934 M8 Bihar-Nepal quake (*Bilham*, 2003).

The Himalayan front is also recognized as a region of unusually high landslide hazard. Steep topographic relief, intense precipitation, and high population density combine with the seismic potential to produce a frequent occurrence of fatal landsliding. Most non-seismic landsliding occurs during the summer months, when heavy monsoon rainstorms destabilize slopes and trigger failures (*Petley*, 2012). Heavy landsliding in association with past earthquakes has been documented along the Himalayan thrust, including the 1934 M8 Bihar-Nepal quake (*Pandey and Molnar*, 1988), the 1950 Assam quake (*Mathur,* 1953), and the 2005 Kashmir quake (*Owen et al.,* 2008).

The April 25 M_w 7.8 event ruptured approximately a 140 km east-west segment of the Main Himalayan Thrust (MHT), but did not produce a surface break (*Hayes et al.,* 2015). The rupture initiated near Barpak, ~80 km northwest of Kathmandu and propagated eastward. The event was followed by a series of large aftershocks, including a M_w 7.2 event on May 12 which ruptured a portion of the MHT directly east of the April 25 rupture (*Avouac et al,* 2015). Nearly 10,000 fatalities, and economic losses equivalent to billions of US dollars, occurred from the mainshock alone (*Zhao*, 2015). Due to the magnitude of the event, and the proximity of the rupture plane to the surface, extensive landsliding was anticipated from this earthquake.

Immediately after the event, various international groups began working to identify landslides triggered by the quake for disaster-relief and early scientific purposes. Different groups have made conflicting claims on the size of the event; *Kargel et al.* (2016) used mapping based on satellite imagery to identify 4,312 landslides triggered by the quake, and characterized the event as being much smaller than that observed for other comparable

earthquake events. However, *Collins and Jibson* (2015) estimated that the earthquake had triggered tens of thousands of landslides, based on field-based surveys. A region of high-density landsliding was noted mainly in the Greater Himalaya by *Kargel et al.* and the EWF (Earthquakes Without Frontiers) group. *Kargel et al.* suggested that this concentration of landslides was caused by the downdropping of the Greater Himalaya during the earthquake, as well as the abundance of steep slopes in the Greater Himalaya.

Methods

Coseismic landslides were mapped as part of a rapid response award from the National Science Foundation (RAPID EAR – Geomorphology and Land Use Dynamics). This mapping superseded immediate response and recovery efforts comprised of point identification of landslide locations (*ICIMOD*, 2015; *Kargel et al.*, 2015) or lines (*EWF* 2015). High-resolution imagery from the NGA (National Geospatial Agency) was processed and made available within a few months after the event through a cooperative agreement with the NSF-sponsored PGC (Polar Geospatial Center). We examined pre- and post-earthquake orthorectified and georeferenced images in order to visibly identify coseismic landslides.

The availability of high-resolution, high-quality image enabled mapping landslides in detail. Scar (source) areas and deposit (runout) areas can be differentiated, allowing us to create the first polygon inventory for a coseismic landslide event with such delineation. In addition, we calculated various statistics that could be used to quantify the mobility of landslides, using SRTM 30-m resolution digital topography.

Landslide inventory

Coseismic landslides were mapped by comparison of pre- and post-event high-resolution (<1m) satellite photographs. Images used were visible-light and panchromatic images collected by the Worldview satellites, which were pansharpened and orthorectified by DigitalGlobe. The Worldview satellite imagery provides image resolutions of <0.5 m. Acquisition dates of imagery used to map landslides ranged from May 2 to June 6, as continuous cloud cover was present for the first week following the main shock. When multiple sets of imagery from different dates were available for an area, the least distorted imagery was used to map polygons; other sets of earlier imagery were sometimes used to better constrain the formation date of a landslide when possible, but were not used to map features if they were more severely distorted than later sets.

Landslide areas were outlined manually onto the georeferenced imagery as polygon features using ArcMap v. 10.2.2 (ArcInfo, ESRI). Small landslides were recognized by changes in reflectivity due to surface disruption or loss of vegetative cover, and larger landslides could be identified by fresh morphologic features (i.e. scarp, toe, etc.). Fresh landslides, as well as, pre-existing landslides reactivated in the post-event images were mapped and included in the inventory. Landslides as small as ~100 m^2 in total area could be recognized across much of the study area. Manual methods were used rather than automated or semi-automated methods, because automated methods produce large numbers of false positives in the mapped inventory. Therefore, manual techniques, despite being labor-intensive, are still considered to yield the highest-fidelity mapping results (*Harp and Jibson*, 1996; *Harp et al.,* 2011; *Xu et al*, 2014).

Where landslides were partially obscured by clouds or steep terrain, polygons were drawn around the visible portion of the landslide and marked as incomplete. Clouded areas, and areas shadowed by steep slopes, were marked and excluded from calculations which are dependent on mapped area such as landslide density (purple polygons, Fig. 1B). Image distortions also limited the mapping area, as severely distorted images provide an

inaccurate representation of landslide geometry. Landslides might also be mislocated in distorted imagery relative to their actual locations on reference terrain models (such as SRTM digital topography), and would contribute potentially erroneous statistical values with respect to topographic variables (i.e. slope, elevation, etc.).

Combining adjacent landslides into single polygon features, or "amalgamation" is known to skew landslide inventory statistics. In order to minimize such effects, adjacent landslides with separate source areas were mapped as separate polygons to the greatest extent possible. When deposits from multiple source areas overlapped, the deposit was assigned only to the largest contributing source area, to prevent double counting of deposit areas in the inventory.

Fresh landslides were most easily recognized by the changes in spectra associated with vegetation loss. The lack of vegetation at high elevations in the Himalaya thus made mapping more difficult, although fresh landslides could still generally be recognized by more subtle changes in reflectivity or morphology. Snow cover could also potentially obscure some landslides, although generally deposits from fresh landslides were observed on top of the snow cover, rather than beneath. Nevertheless, these issues that the higher elevations are more biased more towards minimum estimates of landsliding, as compared to vegetated areas at lower elevations.

Cloudy weather frustrated early efforts to obtain satellite imagery of affected areas in the days immediately after the event; as a result of this it is possible that some mapped landslides may have been triggered by aftershocks within the first week following the event, rather than the mainshock. However, we note that most of our inventory is derived from post-event imagery that predates the M_w7.2 aftershock on May 12. While we cannot rule out contributions to landsliding from several >M6 aftershocks which occurred in the two days following the mainshock, we can see that many of the larger aftershocks (including the M_w7.2 event on May 12) contributed little to observed landsliding. This notion was also corroborated by ground reports from affected areas. The extent of areas mapped to date is shown in Fig. 1B.

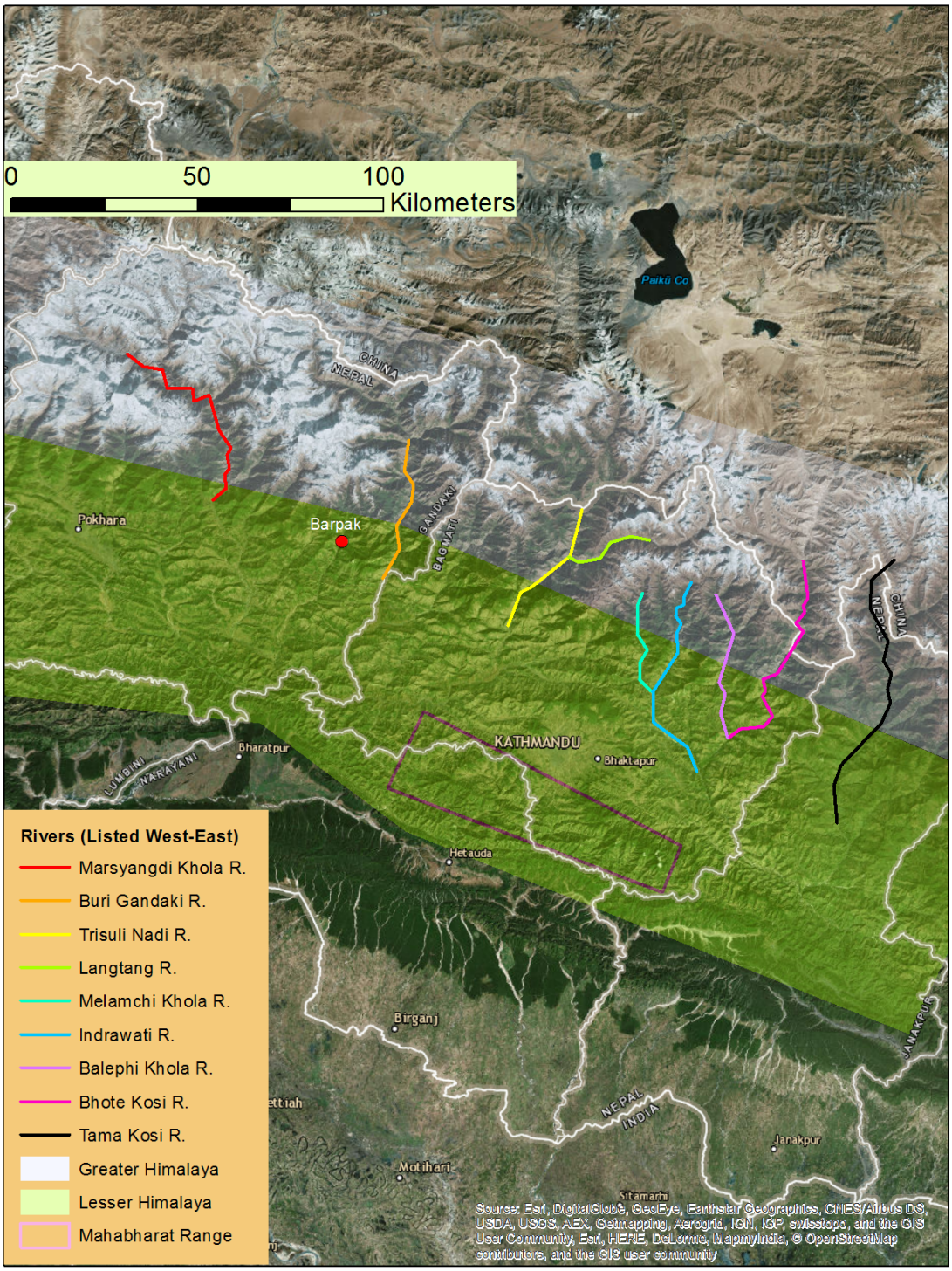

Fig. 1A: View of the study area, with major physiographic provinces, river valleys, and some cities labeled.

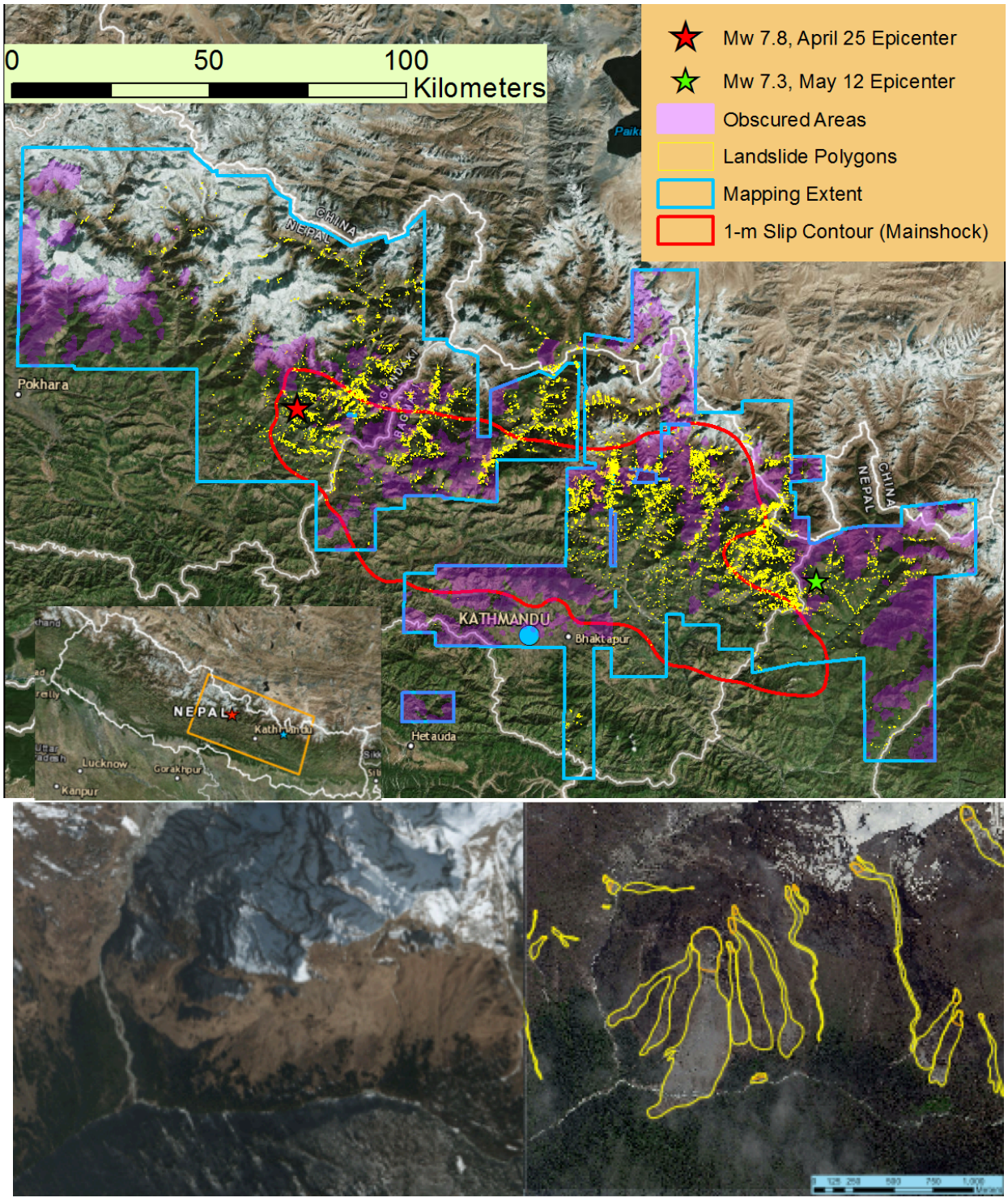

Fig. 1B (Top): Wide view of mapping areas in relation to the April 25 rupture area (with inset map showing wider extent of the study area). **Bottom:** Sample of landslide mapping in the upper Balephi Khola watershed showing pre-earthquake conditions (left) and post-earthquake landslides (right). Polygons identify total landslide areas (yellow) and scars (orange).

Landslide statistics

Several types of landslide statistics were calculated using ArcInfo tools and STRM (Shuttle Radar Topography Mission) digital topography. The STRM project used radar interferometry to create a digital elevation model (DEM) of the entire Earth at 1 arc-second (~30-m) resolution (*Farr et al,* 2007). Topographic data for our studied area from this project was downloaded and projected into the WGS (World Geodetic System) 1984 Zone 45N coordinate system, to align with the coordinate system used in mapping the landslide polygons. A slope grid of equivalent resolution was calculated and minimum, maximum, and average slopes and elevations were extracted for the areas enclosed by individual mapped landslide polygons including separation of source and runout area.

The coarse resolution of our DEM proved to be a major limiting factor in our analysis. While the high-resolution imagery enabled mapping of many small (~100 m^2 or smaller) landslides, accurate characterizations of elevation and particularly slope were not always possible for such small features. Additionally, estimated PGA from the main April 25 event at each feature was calculated using the latest version of the USGS ShakeMap for that event (*USGS*, 2015).

Additional statistical properties of the landslide inventory include landslide volume, runout length, and potential energy of the source volume. Landslide volume was calculated using the area-volume relation given in *Parker* (2011) for mixed Himalayan bedrock and soil landslides:

$$Volume = 0.257(Area)^{1.36}$$

Runout length was estimated using an assumed simple geometry of the landslide with a circular source area and straight runout path of constant width. Under this geometry, the runout length could be related to the source area and full area statistics:

$$R = \frac{2A_F}{\sqrt{\pi}\sqrt{A_S}}$$

Here, R is the runout length, A_F is the full area (source and runout) affected by the landslide, and A_S is the source area. Potential energy was calculated as:

$$E = \rho g H v$$

Here, ρ is the density of the source mass (assumed to be 2500 kg/m^3), g is gravitational acceleration, H is the height drop (difference in height between the highest and lowest elevation included in the full mapped polygon), and v is the source volume).

Using these calculated quantities, the relative mobility of landslides in the inventory could be quantified. Landslides with source areas of less than 900 m^2 (equivalent to the size of one DEM pixel) were excluded from mobility calculations (except where noted), as the coarse resolution of our DEM could lead to inaccurate representations of slope angles, especially for smaller features. We define a relatively mobile landslide as a runout length to height drop (R/H) ratio > 2, which is a value that exceeds typical volume to mobility relationship for this dataset.

Results and Discussion

Upwards of 22,000 landslides triggered by the Gorkha earthquake have been mapped to date. Small gaps in our mapping remain because of the lack of undistorted imagery in these regions including areas due north of Kathmandu, in the southern Lesser Himalaya (Mahabharat Range) and a portion of the Greater Himalaya, which encompasses the upper Trisuli River drainage (Fig. 1A, 1B). However, we interpret low landslide densities in these regions based on mapping in adjacent areas and from regional point and line inventories (*EWF,* 2015; *Kargel et al.,* 2016). For this reason, we consider the inventory to be largely complete, and that we have identified and mapped most of the high-density regions of landsliding associated with this event. *Malamud and Turcotte* (2004) published a relation between earthquake moment magnitude and the number of landslides triggered by the earthquake, based on a study of previously compiled coseismic landslide inventories. The count of ~22,000 landslides mapped in association with the Gorkha earthquake is in good agreement with this relation.

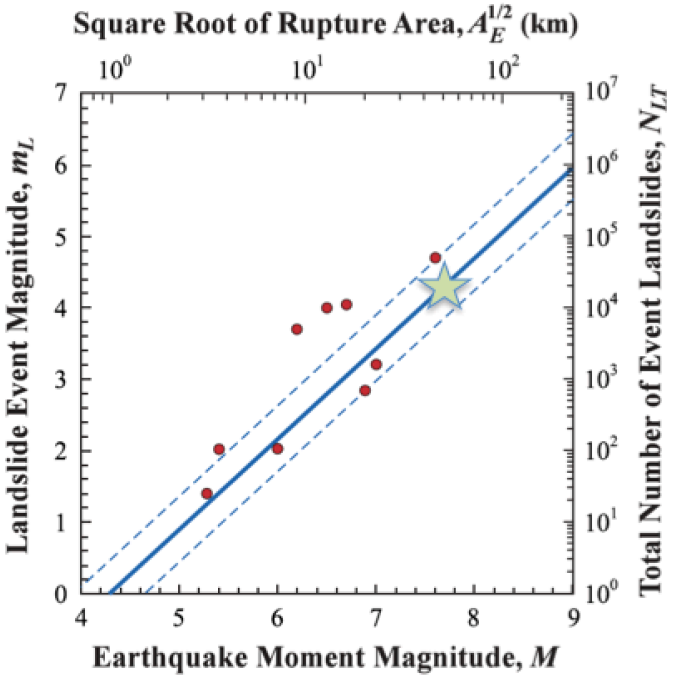

Fig. 2: Fig. 4 modified from *Malamud and Turcotte* (2004) to include the Gorkha landslide inventory (green star).

A comparison of our inventory to other coseismic landslide inventories (in frequency-area space) is given in Fig. 3A. The distribution peaks at landslide areas around 10^3 m^2. In Fig. 3B, the plot is normalized for the varying sizes of the landslide inventory. The Gorkha landslide inventory plots most closely to the Northridge inventory. This may reflect the higher quality of imagery used to create these inventories. There is also a relative lack of larger landslides in the mapped inventory, in comparison to the ChiChi and Wenchuan events, consistent with field observations (*Collins and Jibson*, 2015).

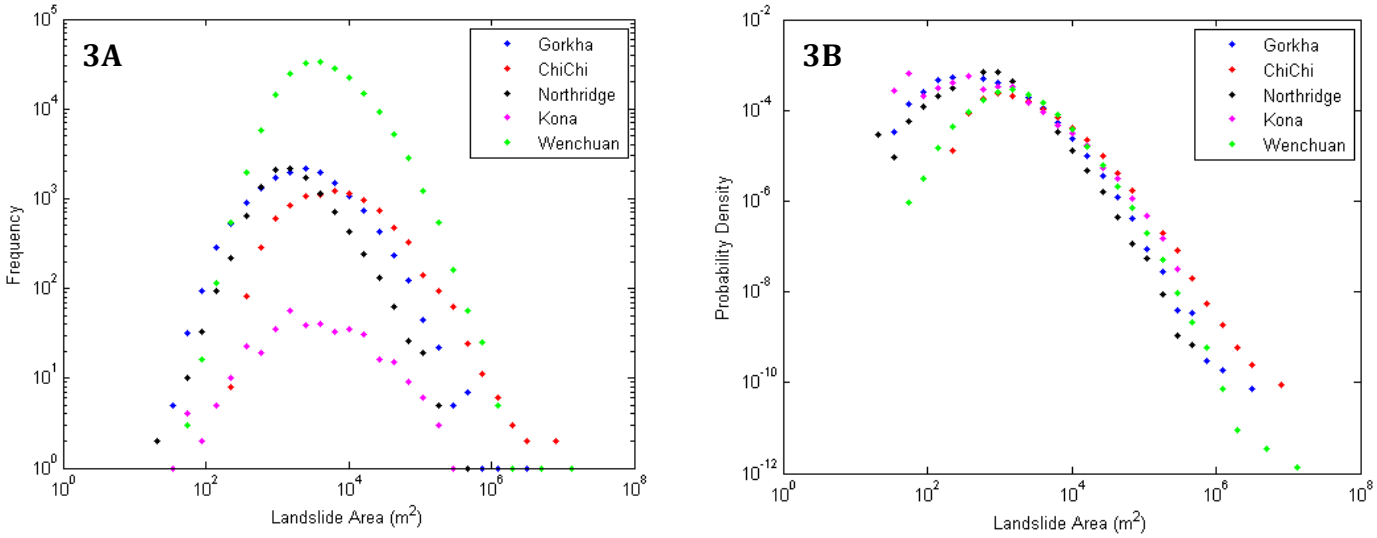

Fig. 3: Frequency-area (3A) and probability density-area (3B) plots for 5 coseismic landslide inventories: Gorkha (2015), ChiChi (1999), Northridge (1994), Kona (2006), and Wenchuan (2008).

We analyzed the landslide distribution with respect to trends in elevation, rupture direction and mobility as detailed in the following sub-sections. General patterns include a concentration of landsliding at lower elevations (below 3500 m) in deep Greater Himalayan river gorges. Few landslides were found in the higher, glaciated terrain despite much higher steep slopes concentrated there. The landslide distribution also showed an eastward focus, with the highest densities found above the eastern end of the fault rupture area. The mobility of landslides was also studied; we found that the most mobile landslides generated by the Gorkha quake tended to occur at high elevations in the Greater Himalaya.

Landslide distribution with respect to elevation

High-density regions of landsliding were generally found to occur at lower elevations in the Greater Himalaya. The highest regions of landslide density occur between elevations of 1500 and 3500 m in the Greater Himalaya specifically in the main trans-Himalyan river gorges (Fig. 4 and 5). Relatively few landslides were found in the higher, glaciated terrain of the Himalaya. However, forward prediction models of slope failures based on model PGA, local slope and a uniform rock strength predict the opposite pattern (higher density landsliding at high elevation) because of the steeper topography in the high elevation, glaciated terrain (*Gallen et al.*, in review). This discrepancy between the predicted and observed distribution can be explained by a number of different factors.

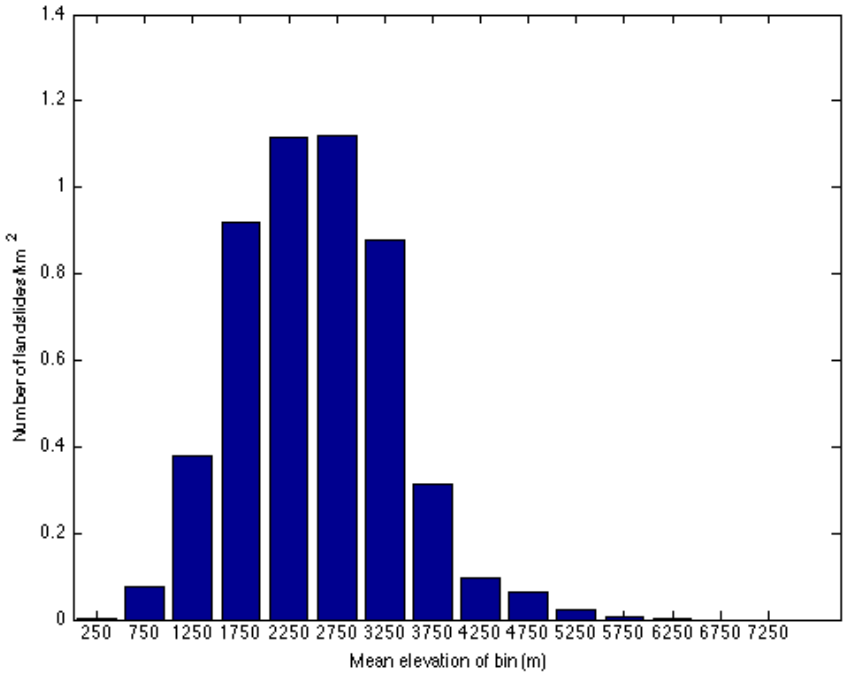

Fig. 4: Landslide density as a function of elevation. Landslide density is concentrated between 1500-3500 m elevation.

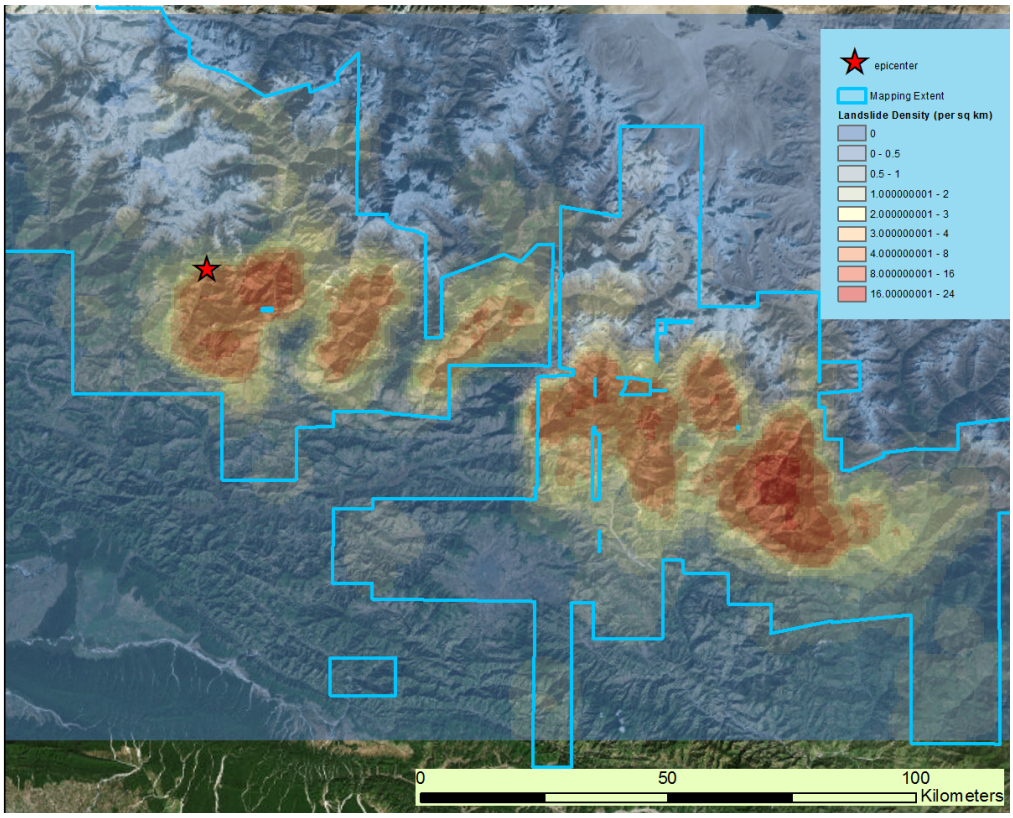

Fig. 5: Map of landslide density resulting from the Gorkha earthquake.

Important factors in influencing coseismic landslide distributions include the nature of the earthquake source, local variations in PGA (Peak Ground Acceleration) driven by local geology and/or topography, variations in the susceptibility of different slopes to failure. Of

these factors, the first we investigated was variation in slope susceptibility with elevation. Slope susceptibility is a function of slope steepness, the strength of the slope-forming material (soil, regolith and/or underlying bedrock), and groundwater presence/flow. However, because the earthquake occurred near the end of the dry season, we neglected consideration of possible groundwater and precipitation effects.

Not surprisingly, landslide density is a strong function of slope, with the majority of landslides occurring on slopes greater than 40 degrees (Fig. 6). Using the 30 m SRTM DEM, both the relative abundance of steep slopes (> 40°) and mean slope increase at higher elevation (Figs. 7 and 8). Therefore, steep slopes are more abundant at high elevations in the Greater Himalaya than they are at lower elevations, where landsliding is more densely concentrated. This indicates that another factor other than slope steepness is needed to explain the observed landslide distribution.

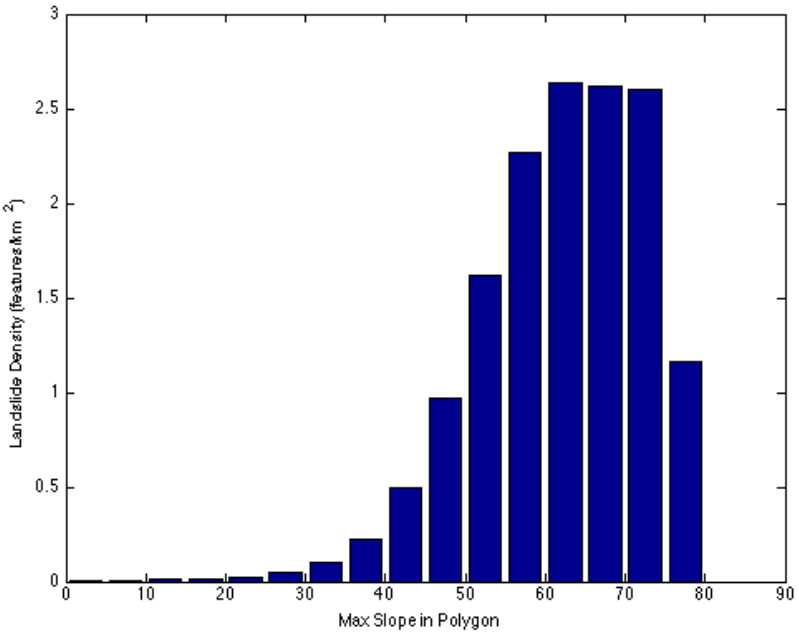

Fig. 6: Landslide density as a function of slope. Maximum slope within the landslide polygon is used as a proxy for the likely initiation of failure.

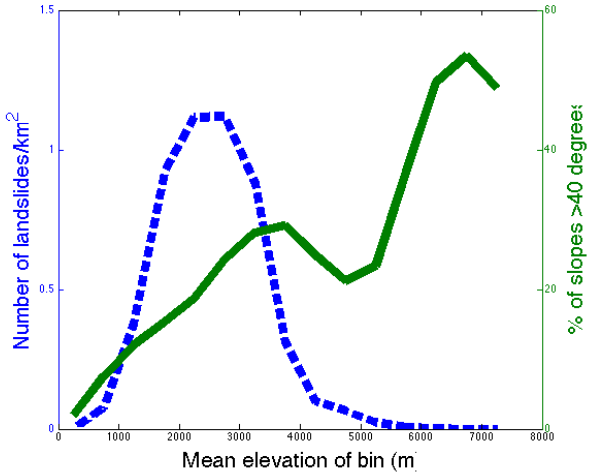

Fig. 7: Landslide density (dashed line), and percent abundance of steep slopes (solid line), plotted as a function of elevation in the study area as given in Fig. 1.

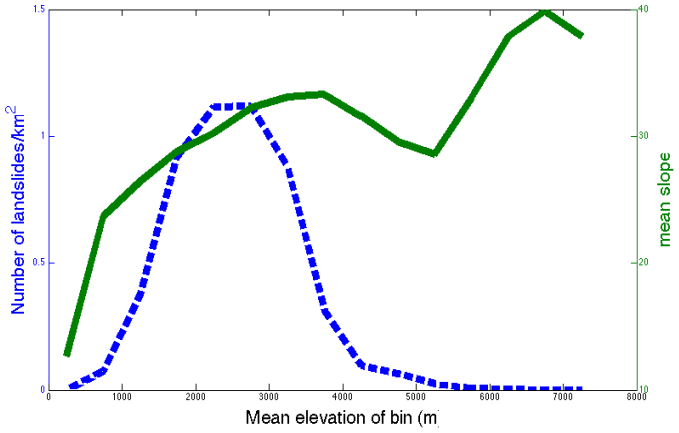

Fig. 8: Landslide density and mean slope, plotted against elevation in the study area as given in Fig. 1.

Variations in rock strength could explain the observed patterns of landslide density with respect to elevation. Although the subject has not been studied extensively in the Himalaya, one might expect greater rock strength at high elevations due to a relative lack of chemical weathering and soil formation in glaciated terrain. Alternatively, local variations in PGA could exist due to interactions with topography. The interaction of incoming seismic waves with the Earth's surface can produce complex patterns of interference, leading to unexpected amplification or damping of shaking in local areas. Upslope amplification of seismic shaking has been observed at some sites (e. g., *Sepúlveda et al.,* 2005; *Hough et al.,* 2010), but generalized patterns of amplification are not well understood for the litany of varying topographies and subsurface structures that are observed in natural hillslopes. If this effect applies to the Gorkha event, we would expect systematic variations in PGA due to the shape of glacial versus fluvial topography.

Landslide distribution with respect to rupture propagation

The landslide inventory also shows an eastward-directed focusing of landslide activity, which clearly predates the May 12 M_w7.2 aftershock located at the eastern terminus of the main shock rupture area (Fig. 9). A peak in landslide density occurs near the epicentral region; landslide density then falls east of the epicenter, and trends back upward toward the eastward end of the rupture area. The highest peak in density occurs just east of the termination of the mainshock rupture, corresponding to the Bhote Kosi river area. The decline of landslide activity east and west of the rupture respectively are startlingly different; landslide density decreases more rapidly to the west than the east. This trend may reflect a greater intensity of shaking or higher frequency spectra in the direction of rupture propagation for the earthquake.

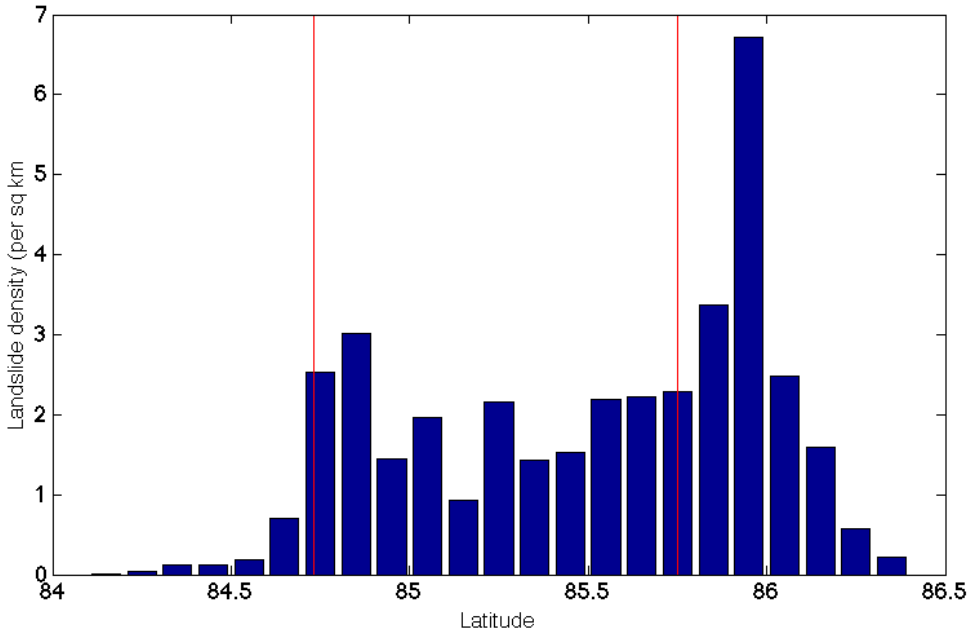

Fig. 9: Mapped landslide density, plotted against longitude. Surface projection of the fault rupture area are shown by the vertical red lines.

Landslide distributions are potentially influenced by aftershock activity. Comparison of imagery sets collected on May 3 and May 25 of the highest-density areas of landsliding in the Bhote Kosi suggests that the M_w 7.2 aftershock triggered very minimal landslide activity (Fig. 10). Ground reports corroborate with the notion that most landsliding was triggered by the mainshock rather than aftershocks. This may indicate that the April 25 mainshock effectively cleared most unstable material off of slopes in the affected region, leaving little for subseqent aftershocks to move in such a short time period. Smaller aftershocks also are unlikely to contribute to further landsliding since generally M4 and greater earthquakes are required to trigger landsliding (*Malamud and Turcotte,* 2004).

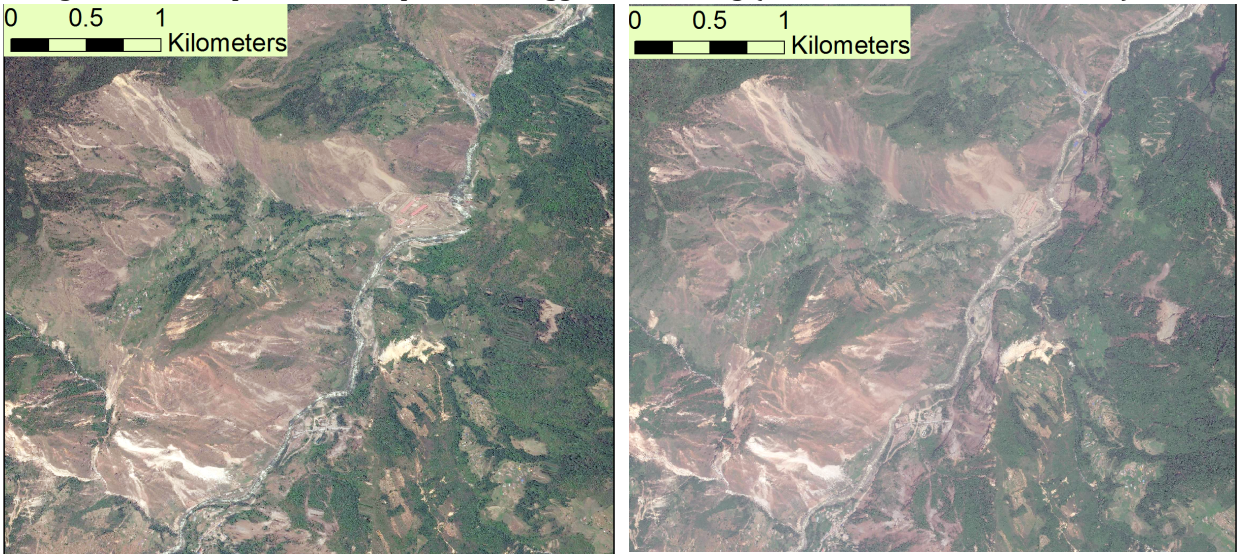

Fig. 10: Comparison of imagery taken May 3 (left) and May 25 (right) in the Bhote Kosi river area (~27.91 N, 85.92 E).

Landslide mobility

We observe that large source volumes tend to be relatively more mobile than smaller ones, consistent with a well-recognized "size effect" observed in other datasets (Fig. 10; e.g. *Dade and Huppert*, 1998). The main population of landslides is concentrated at low source volumes (~10^3 m^3) and low (≈0.1-0.3) values of R/H; however, larger source volumes of around 10^4 m^3 or greater tend to have R/H values near 0.5. Interestingly, there is not a continued increase in mobility of landslides for source areas reaching into the 10^5 to 10^6 m^3 range. This could reflect a limitation of landslide transport by hillslope length in the Himalaya; since most landslides happen at lower elevations in the Greater Himalaya, they might be stopped quickly when they reach the bottom portions of narrow river gorges.

Larger source areas might be favored at higher elevations due to the fact that landslides at higher elevations are more likely to be rock slides than those at lower elevations (due to a lack of presence of soils and chemical weathering at high elevations). Failures in rock slides are controlled primarily by fractures and joints, which have a lower effective strength at larger scales (*Bandis et al.,* 1981; *Hoek and Brown*, 1997); this favors larger failures in fractured rock masses, as opposed to smaller failures in soil and variably weathered regolith.

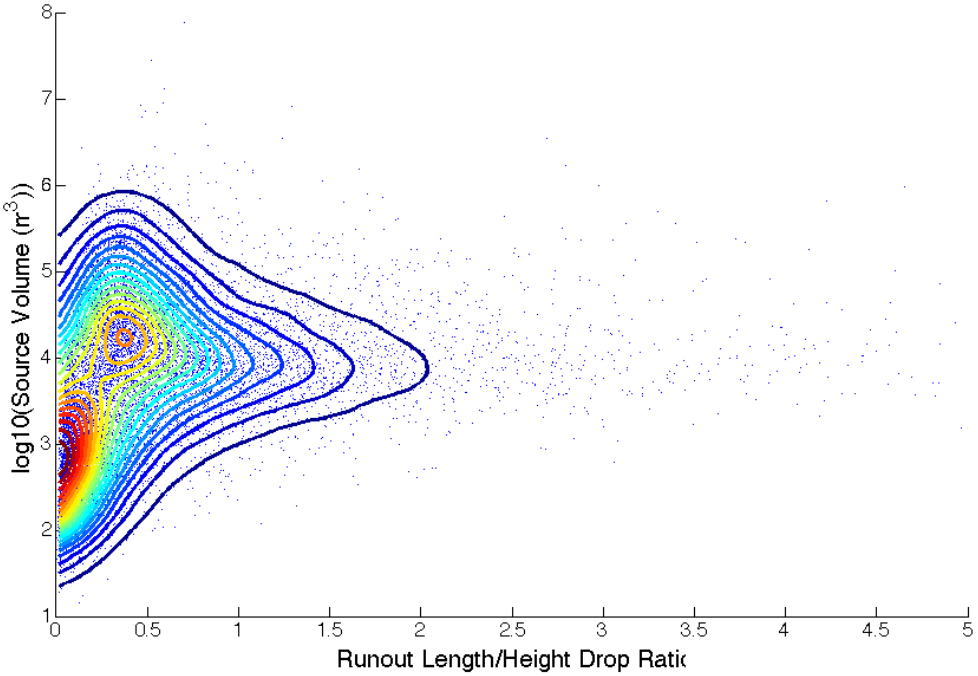

Fig. 11: Plot of R/H against estimated source volume for mapped landslides from the Gorkha earthquake. Plot is contoured by point density.

We also isolate a subset of particularly mobile landslides, which do not follow the expected size-mobility trend. These were defined as those landslides which had a source area greater than 900 m^2, a runout length greater than 200 m, and a runout length to height drop ratio greater than 2. In Fig. 12, the count of these landslides is plotted against elevation. In sharp contrast to the main distribution, highly mobile landslides are most abundant at higher elevations (peaking at ~4500 m), in the glaciated parts of the Greater Himalaya.

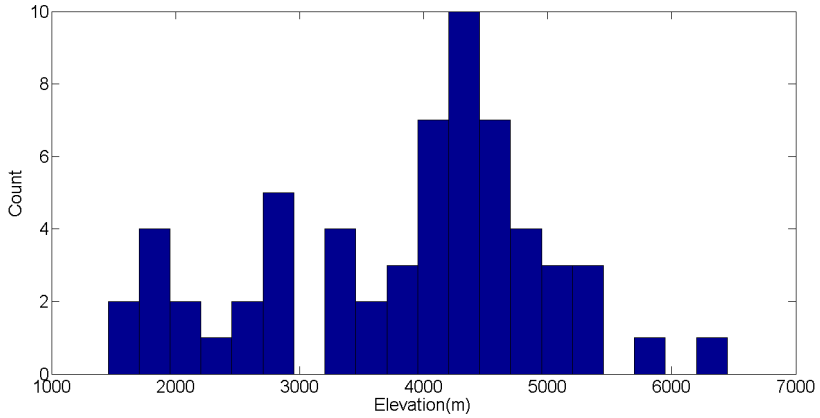

Fig. 12: Count of high-mobility landslides triggered by the Gorkha earthquake, plotted against elevation.

One factor that may enhance high-elevation landslide mobility is lower frictional resistance to landslide movement. At high elevation in the Greater Himalaya, vegetation is sparse to nonexistent, and snow, ice, and bare rock are the dominant surface-forming materials. At lower elevations, dense forests and unconsolidated soils mantle the surface and these might be expected to impede the movement of a landslide mass more than the smoother surfaces found at high elevations. If snow and ice mix into the moving material and are melted due to frictional heating, they could also serve as a fluidizing medium for the moving mass, increasing its mobility (e. g., *Legros,* 2002).

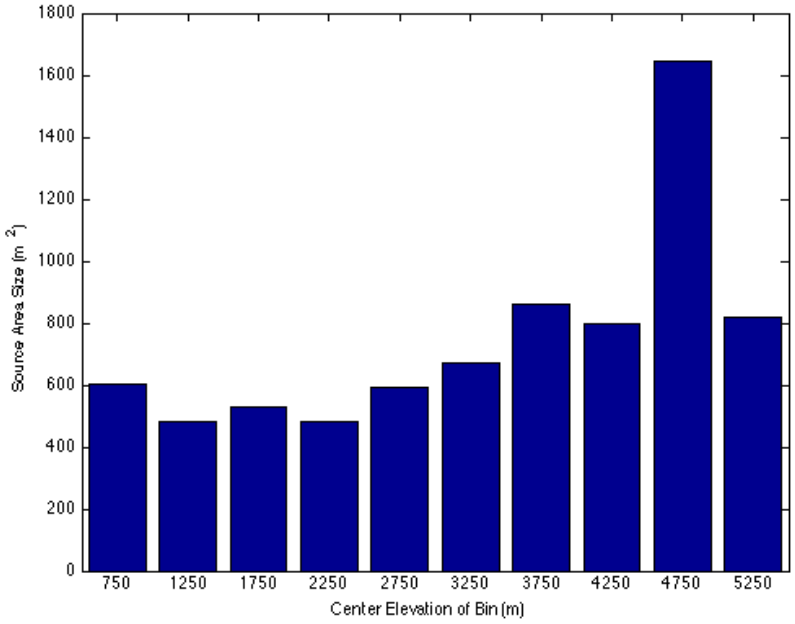

Fig. 13: Average source area size for landslides triggered by the Gorkha earthquake, plotted against elevation.

Steeper slopes and cliffs at high elevations (Fig. 8) could also contribute to the high mobility of landslides, since a steeper slope provides a clearer path of descent and faster acceleration of the slide mass than a shallower one. Additionally, the presence of steeper slopes could also encourage the detachment of larger, more mobile source volumes in

failure events. Longer hillslope lengths in the high Himalaya, if present, could also enhance landslide mobility.

Conclusions

The April 25, M_w 7.8 Gorkha earthquake triggered upwards of 22,000 landslides. The number of mapped landslides is in good agreement with that predicted by previously published relations between an earthquake moment magnitude and coseismic landslide count. Higher concentrations of landslides were observed at lower elevations in Greater Himalayan river gorges, despite greater steep slope distributions at high altitude. Because slope angle variations do not explain the observed distribution of landsliding with elevation, we propose that variations in rock strength and possibly local variations in PGA due to topographic effects dictate the observed landslide distribution. Future field-based studies of rock strength and modeled ground motions that include the effect of topography are required for further understanding.

Landslide density also increases towards the eastern end of the rupture patch. Although this increase correlates with an increase in aftershock density, based on available imagery and ground reports it seems that aftershocks triggered very few landslides in densely-affected areas. We therefore suggest that the increase in density may reflect a focusing of seismic energy from the quake in the direction of rupture propagation.

Our studies of landslide mobility found that larger landslides have a tendency to be more mobile than smaller landslides, consistent with the known "size effect" where larger landslides travel greater relative distances (Legros, 2002). We also find that more mobile landslides tend to occur at higher elevations in the Greater Himalaya. This may reflect lower frictional resistance to landslide movement at higher elevations (due to the presence of snow and ice), a preference for larger source areas at high elevations, or increases in hillslope steepness and length.

Acknowledgments

Thanks to Marin Clark for guiding this work and providing countless edits and major fixes to this thesis, and also to Josh West, Dimitrios Zekkos, Sean Gallen, and Jonathan Godt for providing advice and guidance. Funding was provided through the National Science Foundation Rapid Response Award from Geomorphology and Land Use Dynamics (#F039659) to Professor Marin Clark. Thanks also to many family and friends (from both Earth & Environmental Sciences and elsewhere) who have lent personal support over the last few years!

References

Avouac, J. P., Meng, L., Wei, S., Wang, T., and Ampuero, J. P., 2015, Lower edge of Main Himalayan Thrust unzipped by the 2015 Gorkha earthquake: Nature Geosciences, doi:10.1038/NGEO2518.

Bandis, S., Lumsden, A. C., and Barton, N. R., 1981, Experimental Studies of Scale Effects on the Shear Behaviour of Rock Joints: International Journal of Rock Mechanics and Mining Sciences & Geomechanics, v. 18, no. 1, p. 1-21, doi:10.1016/0148-9062(81)90262-X.

Bilham, R., 2004, Earthquakes in India and the Himalaya: tectonics, geodesy, and history: Annals of Geophysics, v. 47, p. 839-858.

Collins, B. D., and Jibson, R. W., 2015, Assessment of Existing and Potential Landslide

Hazards Resulting from the April 25, 2015 Gorkha, Nepal Earthquake Sequence, USGS Open-File Report 2015-1142.
Dade, W. B., and Huppert, H. E., 1998, Long-runout rockfalls: Geology, v. 26, no. 9, p. 803-806.
Densmore, A. L., Anderson, R. S., McAdoo, B. G., and Ellis, M. A., 1997, Hillslope Evolution by Bedrock Landslides: Science, v. 275, p. 369-371, doi:10.1126/science.275.5298.369.
Earthquakes Without Frontiers, 2015, UPDATED (30 June) landslide inventory following 25 April and 12 May earthquakes: Earthquakes Without Frontiers Blog, http://ewf.nerc.ac.uk/2015/06/30/updated-30-june-landslide-inventory-following-25-april-and-12-may-nepal-earthquakes/
Farr, T. G., et al., 2007, The Shuttle Radar Topography Mission, Reviews of Geophysics, v. 45, no. 2, doi:10.1029/2005RG000183.
Gallen, S. F., Clark, M. K., and Godt, J. W., 2015, Coseismic landslides reveal near-surface rock strength in a high-relief, tectonically active setting: Geology, v. 43, p. 11-14, doi:10.1130/G36080.1.
Gallen, S. F., Clark, M. K., Godt, J. W., Roback, K., Niemi, N. A., in review, Application of a Rapid Response Earthquake-Triggered Landslide Model to the 25 April 2015 M_w 7.8 Gorkha earthquake, Nepal: Tectonophysics.
Harp, E. L., and Jibson, R. W., 1996, Landslides triggered by the 1994 Northridge, California, earthquake: Bulletin of the Seismological Society of America, v. 86, S319-S322.
Harp, E. L., Keefer, D. K., Sato, H. P., and Yagi, H., 2011, Landslide inventories: The essential part of seismic landslide hazard analyses: Engineering Geology, v. 122, no. 1-2, p. 9-21, doi:10.1016/j.enggeo.2010.06.013.
Hayes, G. P., Briggs, R. W., Barnhart, W. D., Yeck, W. L., McNamara, D. E., Wald, D. J., Nealy, J. N., Benz, H. M., Gold, R. D., Jaiswal, K. S., Marano, K., Earle, P. S., Hearne, M. G., Smoczyk, G. M., Wald, L. A., and Samsonov, S. V., 2015, Rapid Characterization of the 2015 M_w 7.8 Gorkha, Nepal, Earthquake Sequence and Its Seismotectonic Context: Seismological Research Letters, v. 86, p. 1557-1567, doi:10.1785/0220150145.
Hoek, E., and Brown, E. T., 1997, Practical estimates of rock mass strength: International Journal of Rock Mechanics and Mining Sciences, v. 34, p. 1165-1186, doi:10.1016/S1365-1609(97)80069-X.
Hough, S. E., Friberg, P. A., Busby, R., Field, E. F., Jacob, K. H., and Borcherdt, R. D., 1990, Sediment-induced amplification and the collapse of the Nimitz Freeway: Nature, v. 344, p. 853-854.
Hough, S. E., Altidor, J. R., Anglade, D., Given, D., Janvier, M. G., Maharrey, J. Z., Meremonte, M., Mildor, B. S., Prepetit, C., and Yong, A., 2010, Localized damage caused by topographic amplification during the 2010 M 7.0 Haiti earthquake: Nature Geoscience, v. 3, p. 778-782, doi:10.1038/NGEO988.
Huang, R., and Fan, X., 2013, The landslide story: Nature Geoscience, v. 6, p. 325-326, doi:10.1038/ngeo1806.
Kargel, J. S. et al., 2016, Geomorphic and geologic controls of geohazards induced by Nepal's 2015 Gorkha earthquake: Science, v. 351, doi:10.1126/science.aac8353.
Keefer, D. K., 1984, Landslides caused by earthquakes: Geological Society of America Bulletin, v. 95, p. 406-421, doi:10.1130/0016-7606(1984)95<406:LCBE>2.0.CO;2.
Keefer, D. K., 2002, Investigating landslide caused by earthquakes – A Historical Review: Surveys in Geophysics, v. 23, p. 473-510.
Khazai, B., and Sitar, N., 2003, Evaluation of factors controlling earthquake-induced

landslides caused by Chi-Chi earthquake and comparison with the Northridge and Loma Prieta events: Engineering Geology, v. 71, p. 79-95, doi:10.1016/S0013-7952(03)00127-3.

Lavé, J., and Avouac, J. P., 2000, Active folding of fluvial terraces across the Siwaliks Hills, Himalayas of central Nepal: Journal of Geophysical Research Solid Earth, v. 105, p. 5735-5770, doi:10.1029/1999JB00292.

Legros, F., 2002, The mobility of long-runout landslides: Engineering Geology, v. 63, p. 301-331, doi:10.1016/S0013-7952(01)00090-4.

Malamud, B. D., Turcotte, D. L., Guzzetti, F., Reichenbach, P., 2004, Landslides, earthquakes, and erosion: Earth and Planetary Science Letters, v. 229, p. 45-59, doi:10.1016/j.epsl.2004.10.018

Marc, O., and Hovius, N., 2015, Amalgamation in landslide maps: effects and automatic detection: Natural Hazards and Earth System Science, v. 15, p. 723-733, doi:10.5194/nhess-15-723-2015.

Mathur, L. P., 1953, The Assam Earthquake of 15th August, 1950: A Short Note on Factual Observations, *in* Rao, M. B. R. *ed*., A Compilation of Papers on the Assam Earthquake of August 15, 1950, p. 56-60.

Owen, L. A., Kamp, U., Khattak, G. A., Harp, E. L., Keefer, D. K., and Bauer, M. A., 2008, Landslides triggered by the 8 October 2005 Kashmir earthquake: Geomorphology, v. 94, p. 1-9, doi:10.1016/j.geomorph.2007.04.007.

Pandey, M. R., and Molnar, P., 1988, The Distribution of Intensity of the Bihar-Nepal Earthquake of 15 January 1934 and Bounds on the Extent of the Rupture Zone: Journal of Nepal Geological Society, v. 5, no. 1, p. 22-44.

Parker, R. N., Densmore, A. L., Rosser, N. J., de Michele, M., Li, Y., Huang, R., Whadcoat, S., and Petley, D. N., 2011, Mass wasting triggered by the 2008 Wenchuan earthquake is greater than orogenic growth: Nature Geoscience, v. 4, p. 449-452, doi:10.1038/NGEO1154.

Petley, D., 2012, Global patterns of loss of life from landslides: Geology, v. 40, no. 10, p. 927-930, doi:10.1130/G33217.1.

Sella, G. F., Dixon, T. H., and Mao, A., 2002, REVEL: A model for Recent plate velocities from space geodesy: Journal of Geophysical Research Solid Earth, v. 107, ETG 11-1 – ETG 11-30, doi:10.1029/2000JB000033.

Sepúlveda, S. A., Murphy, W., Jibson, R. W., Petley, D. N., 2005, Seismically induced rock slope failures resulting from topographic amplification of strong ground motions: The case of Pacoima Canyon, California: Engineering Geology, v. 80, p. 336-348, doi:10.1016/j/enggeo.2005.07.004.

Tang, N., Zhu, J., Qi, X., and Ding, J., 2011, Landslides induced by the Wenchuan earthquake and the subsequent strong rainfall event: A case study in the Beichuan area of China: Engineering Geology, doi:10.1016/j.enggeo.2011.03.013.

Xu, C., Xu, X., Yao, X., and Dai, F., 2014, Three (nearly) complete inventories of landslides triggered by the May 12, 2008 Wenchuan Mw 7.9 earthquake of China and their spectral distribution statistical analysis: Landslides, v. 11, no. 3, p. 441-461, doi: 10.1007/s10346-013-0404-6.

Zhao, B., 2015, April 2015 Nepal earthquake: observations and reflections: Natural Hazards, v. 80, p. 1405-1410, doi:10.1007/s11069-015-2001-6.